

# Operando MRI for quantitative mapping of temperature and redox species concentrations in thermo-electrochemical cells

Luke O'Dell (✉ [lodell@deakin.edu.au](mailto:lodell@deakin.edu.au))

Deakin University

**Isuru Gunathilaka**

Deakin University <https://orcid.org/0000-0003-1418-6830>

**Jennifer Pringle**

Deakin University <https://orcid.org/0000-0002-2729-2838>

**Maria Forsyth**

Deakin University <https://orcid.org/0000-0002-4273-8105>

---

## Article

**Keywords:** Operando MRI, energy sources, thermo-electrochemical cells

**Posted Date:** June 21st, 2021

**DOI:** <https://doi.org/10.21203/rs.3.rs-568214/v1>

**License:**  This work is licensed under a Creative Commons Attribution 4.0 International License.

[Read Full License](#)

---

**Version of Record:** A version of this preprint was published at Nature Communications on November 8th, 2021. See the published version at <https://doi.org/10.1038/s41467-021-26813-8>.

# Operando MRI for quantitative mapping of temperature and redox species concentrations in thermo-electrochemical cells

Isuru E. Gunathilaka<sup>a</sup>, Jennifer M. Pringle<sup>b</sup>, Maria Forsyth<sup>b</sup> and Luke A. O'Dell<sup>a\*</sup>

<sup>a</sup>ARC Centre of Excellence for Electromaterials Science (ACES), Institute for Frontier Materials, Deakin University, Geelong Waurin Ponds Campus, Victoria 3220, Australia

<sup>b</sup>ARC Centre of Excellence for Electromaterials Science (ACES), Institute for Frontier Materials, Deakin University, Melbourne Burwood Campus, Victoria 3125, Australia

\*Email: [luke.odell@deakin.edu.au](mailto:luke.odell@deakin.edu.au)

**Low-grade waste heat is an abundant and underutilised energy source, and the promise of thermo-electrochemical cells to harvest this resource and power applications such as wearable devices and sensors is increasingly being realised. However, despite substantial advances in performance in recent years, understanding the interior processes occurring within these devices remains a challenge. Here we report an operando magnetic resonance imaging (MRI) approach that can provide quantitative spatial maps of electrolyte temperature and redox ion concentrations in functioning thermo-electrochemical cells. Time-resolved images are obtained from liquid and gel electrolytes, allowing the effects of redox reactions and competing mass transfer effects such as thermophoresis and diffusion to be visualised and correlated with the device performance via simultaneous electrochemical measurements. This method offers valuable insights into these devices and will greatly aid their future design and optimisation.**

## Introduction

As the demand for technology-based solutions to climate change and improved renewable energy sources continues to accelerate, the utilisation of low-grade waste heat becomes increasingly attractive. Such heat is generated by industrial processes, automobiles, natural sources (e.g., solar or geothermal) and even the human body, and represents a vast and largely untapped energy resource [1]. Thermo-electrochemical cells (also referred to as thermogalvanic cells, and hereafter as thermocells) are devices capable of generating electricity from waste heat [2,3]. In their simplest form they consist of two parallel plate electrodes and an electrolyte containing a redox couple with a temperature dependent redox potential. Under an applied thermal gradient, either oxidation or

33 reduction will dominate at the hot electrode depending on the sign of the reaction entropy [4], with  
34 the opposite process occurring at the cold electrode. This generates an electric potential across the  
35 cell (the Seebeck effect), and when an external load resistance is connected to the electrodes the  
36 drawn current will drive further redox reactions, resulting in the continuous generation of power with  
37 no fuel consumption or emissions for as long as the temperature gradient is maintained. Thermocells  
38 have many advantageous features such as no moving parts or potentially deleterious effects such as  
39 plating, stripping, interphase formation or intercalation processes, which will be beneficial for  
40 longevity, and they utilise much lower cost materials than traditional semi-conductor based  
41 thermoelectrics, making them promising for large scale, low cost applications. Recently, significant  
42 progress has been made in developing wearable thermocells to harvest body heat [5-7], as well as in  
43 developing new thermocell designs that incorporate separators or membranes [8], material phase  
44 transitions [9,10], crystallisation processes [11], and improved electrode [12] and electrolyte [13-15]  
45 materials to boost their Seebeck coefficient and efficiency.

46 Despite the simplicity of their design, there are a large number of distinct physical processes  
47 that can occur within the thermocell electrolyte. These include the redox reactions and accompanying  
48 changes in ion clustering and solvation, the establishment of local concentration gradients and  
49 resulting diffusion along these gradients, self-diffusion (due to Brownian motion), thermophoresis  
50 (the migration of species along a temperature gradient, usually from hot to cold, also known as the  
51 Soret effect), electrophoresis (the migration of charged species along a potential) and convection. All  
52 of these processes will be highly inter-dependent, for example convection can be caused by the  
53 applied temperature gradient but also by variations in the electrolyte density resulting from the redox  
54 reactions and concentration gradients. Moreover, these processes will also depend on various  
55 external parameters such as the shape, size and orientation of the electrolyte chamber, and due to  
56 the effects of the chamber walls they will potentially show distinct spatial variations in all three  
57 dimensions. This multitude of interacting factors is complex enough during the steady-state operation  
58 of the device, but they will also vary as a function of the applied thermal gradient and load resistance,  
59 both of which may be time dependent in real-world applications. Understanding and quantifying these  
60 phenomena, their relation to the cell design and their impact on the performance of the device is  
61 therefore a major challenge.

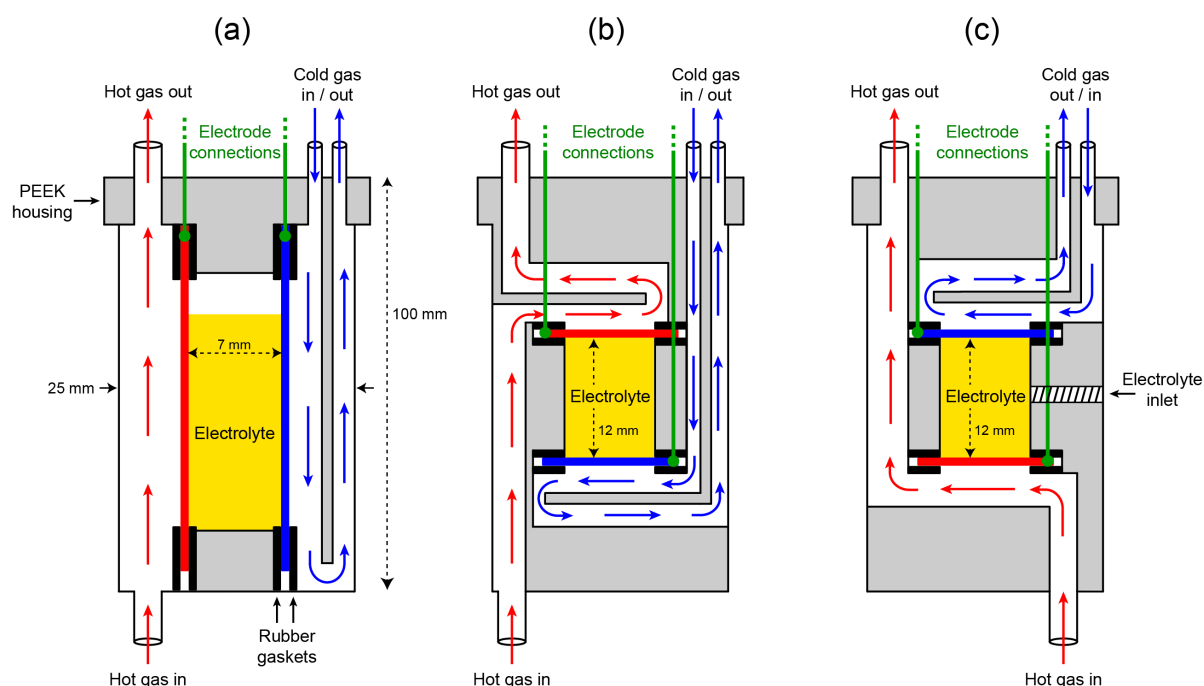
62 Thus far, the most viable way to visualise these processes has been via numerical modelling,  
63 and a number of previous publications have used this approach to predict the spatial variations in  
64 temperature and concentrations of the redox species for cells operating under steady-state conditions  
65 [16,17]. These studies have provided valuable insights, for example Sokirko's model predicted linear  
66 concentration gradients for the redox species in the absence of convection [16], and, when convection

67 is present, the existence of diffusive layers at the electrodes (regions of enhanced concentration of  
68 redox species due to their generation at the electrode surface) with a neighbouring “inversion layer”  
69 showing a reduced concentration of that species relative to the bulk [16,17]. These features are  
70 predicted to be more pronounced at the cold electrode due to the slower local diffusion. Salazar and  
71 co-workers used their model as a basis for the optimisation of cell designs and geometries, and  
72 showed that stacking cells in series could significantly boost conversion efficiency [17]. However, such  
73 models inevitably necessitate various simplifications. For example, Salazar’s model was restricted to  
74 two dimensions, thus could not consider any effects of the interior side walls of the cell, and also had  
75 to neglect the effects of thermophoresis under the assumption that other mass transfer effects are  
76 dominant in a functioning cell [17].

77 To the best of our knowledge, the experimental observation of the various inter-related and  
78 spatially-dependent phenomena occurring in a working thermocell has not yet been achieved. The  
79 vast majority of experimental studies have focused on electrochemical measurements [18] carried out  
80 on thermocells featuring different electrode and electrolyte materials, and with different cell  
81 geometries, orientations and designs [19-24]. While these are extremely useful and can be used to  
82 quantify the device performance, they provide little information on the processes occurring within the  
83 electrolyte and certainly no insights into spatial variations in the cell. Said and co-workers have used  
84 infrared thermal imaging to study the temperature distribution across thermocells incorporating  
85 polymer membranes [25], but these images could only provide the temperature across the outer  
86 surface of the device.

87 Operando magnetic resonance imaging (MRI) is a versatile and non-invasive technique that  
88 has been used by a number of research groups to study energy storage devices such as double-layer  
89 capacitors [26] and batteries [27,28], allowing the mapping of ion concentration gradients in  
90 electrolytes [29-32], studies of device charge state [33] and current distributions [34], and the  
91 observation of processes such as Li and Na ion intercalation into electrodes [35], the growth of metallic  
92 dendrites from the electrode surface [36], and magnetohydrodynamics in the electrolyte [37]. This  
93 technique is particularly well suited for studies of thermocells given the inherent paramagnetic nature  
94 of many redox species that will result in enhanced relaxation-based image contrast [38], as well as its  
95 ability to quantitatively probe translational molecular dynamics including diffusion and flow. To this  
96 end, we have constructed custom thermocells designed specifically for operando MRI characterisation  
97 using a microimaging probe with a 25 mm inner diameter radiofrequency coil (Figure 1). The cell  
98 housing is made of polyether ether ketone (PEEK), an inert material that is easily machined and is  
99 thermomechanically stable. The electrolyte is contained in a central chamber between two 0.25 mm  
100 thick platinum plate electrodes held in place using butyl rubber gaskets. The electrode temperatures

101 are controlled in situ using hot and cold gas streams that flow over the outer surfaces of the electrodes  
 102 and whose temperatures and pressures can be individually controlled. Due to the design of the  
 103 imaging probe used and space restrictions inside the magnet, the hot gas is required to enter the cell  
 104 from below with the other gas connections located at the top. Despite this restriction, the modular  
 105 design of the horizontal electrode cell allows either hot-above-cold or cold-above-hot orientations  
 106 (Figure 1b and 1c). As the electrolyte temperature is measured directly during the experiments via the  
 107 MRI images obtained, no thermocouples are required. Electrode connections are achieved using wires  
 108 extending from the top of the cells and these are connected to a potentiostat located outside of the  
 109 magnet using shielded cables.



110 **Figure 1 – Schematics of the thermocell designs for operando MRI experiments, with (a) vertical, (b)**  
 111 **hot-above-cold and (c) cold-above-hot electrode orientations. Red and blue arrows represent hot**  
 112 **and cold gas flow pathways respectively. Additional illustrations of the cells are provided in the**  
 113 **Supplementary Information, and full design details are available upon request.**

114

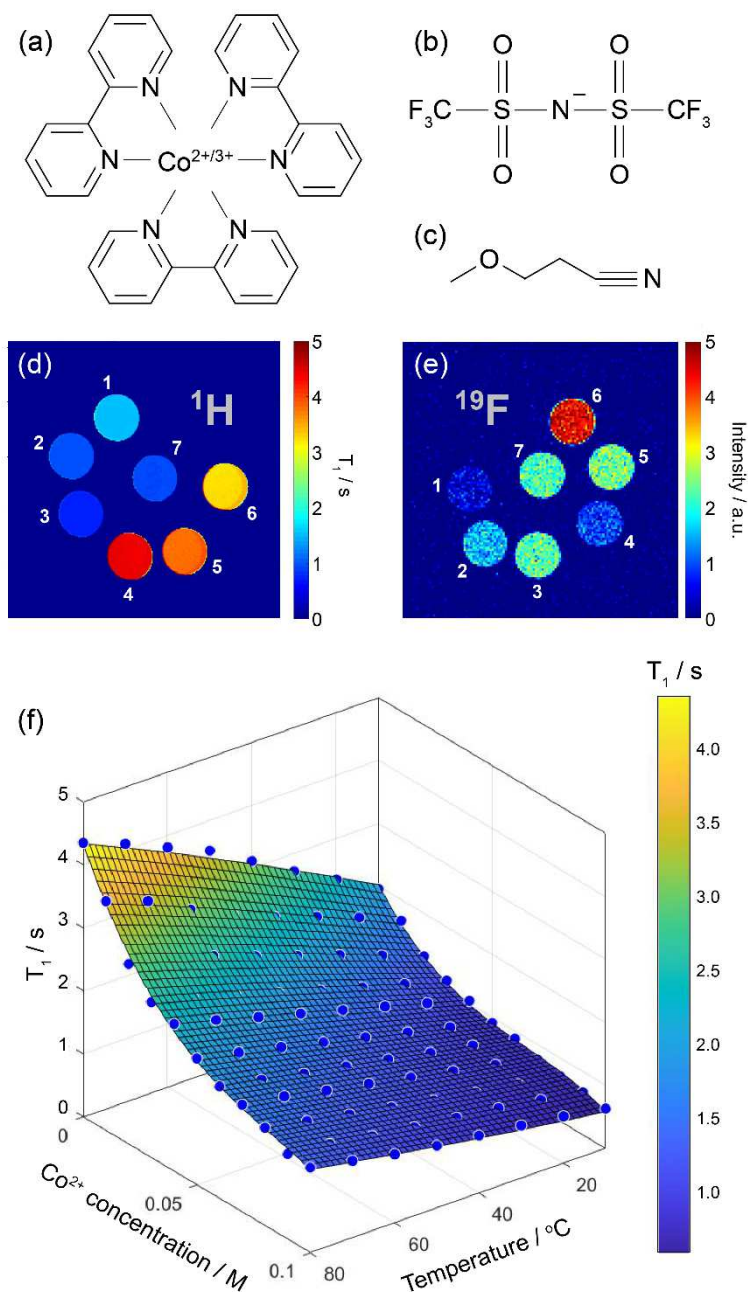
115 The electrolyte system chosen for this work consists of the tris(bipyridyl)cobalt redox couple  
 116  $\text{Co}(\text{bpy})_3$  with the bis(trifluoromethanesulfonyl)-imide (TFSI) anion in the solvent 3-  
 117 methoxypropionitrile (MPN) (molecular structures shown in Figure 2). The cobalt cation can exist in  
 118 either the paramagnetic  $\text{Co}^{2+}$  or diamagnetic  $\text{Co}^{3+}$  oxidation states, with two or three associated TFSI  
 119 anions respectively. This system was chosen based on its relatively high Seebeck coefficient of 1.99  
 120  $\text{mV K}^{-1}$  (measured for an MPN electrolyte containing 0.05 M of both redox species) [21]. A gelled form

121 synthesised by incorporating 5 wt% polyvinylidene difluoride (PVDF) has also been studied previously  
122 [23] and was investigated in this work alongside the liquid form. For this electrolyte, the redox reaction  
123 entropy is positive and thus the hot electrode acts as the cathode and reduction reactions dominate  
124 on that side of the thermocell, forming the paramagnetic  $\text{Co}^{2+}$  state, with the opposite process  
125 occurring at the cold electrode.

126

## 127 **Results**

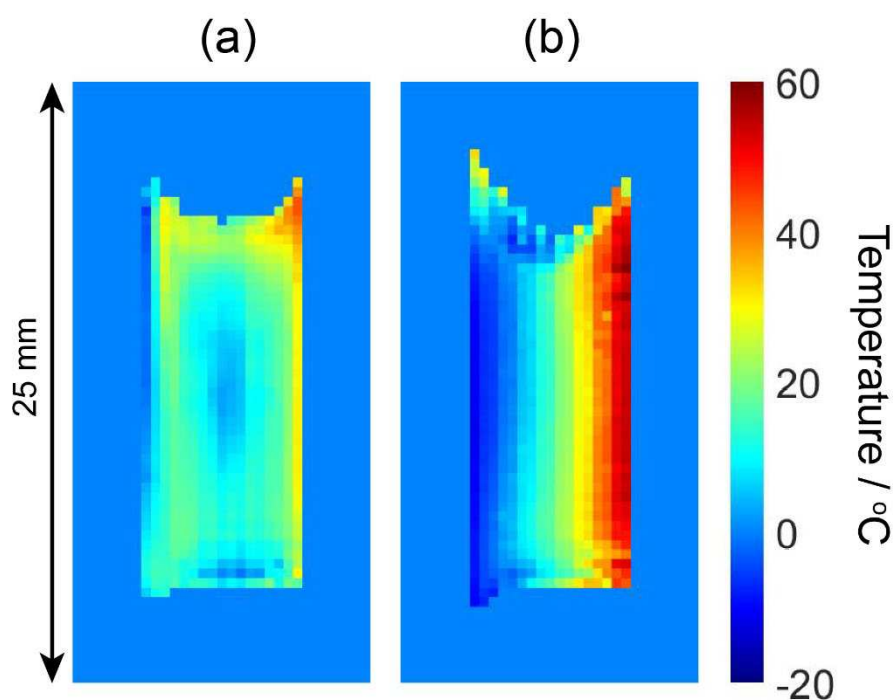
128  **$^1\text{H}$  and  $^{19}\text{F}$  image contrast.** Axial-slice images of liquid electrolyte samples with different  
129 concentrations of each cobalt oxidation state, acquired using the  $^1\text{H}$  nuclei of the MPN solvent  
130 molecules and the  $^{19}\text{F}$  nuclei of the TFSI anions, are shown in Figure 2d and 2e respectively. The  
131 protons of the bipyridyl ligands give well resolved  $^1\text{H}$  NMR signals for the different cobalt oxidation  
132 states due to the large paramagnetic shift induced by the  $\text{Co}^{2+}$  (see Supplementary Information), so  
133 chemical shift selective imaging could in principal be used to directly observe these species. However,  
134 the MPN solvent molecules give  $^1\text{H}$  signals that are approximately two orders of magnitude larger and  
135 so these signals were exploited for the  $^1\text{H}$  imaging. Figure 2d shows that the MPN  $^1\text{H}$   $T_1$  (i.e., the  
136 longitudinal nuclear spin relaxation time, a parameter commonly used to generate MRI image  
137 contrast) is sensitive to the concentrations of both redox oxidation states, while the  $^{19}\text{F}$  spin density  
138 contrast in Figure 2e also reports on these concentrations due to the different relaxation times as well  
139 as the different numbers of anions associated with each cobalt redox state. While both nuclei are  
140 viable for imaging, in the majority of this work we have focused on  $^1\text{H}$  due to its higher sensitivity.



141 **Figure 2 – Molecular structures of (a) the tris(bipyridyl)cobalt cation  $\text{Co}(\text{bpy})_3$ , (b) the**  
 142 **bis(trifluoromethanesulfonyl)-imide anion (TFSI), and (c) the 3-methoxypropionitrile (MPN) solvent.**  
 143 **(d) and (e) show axial slice  $^1\text{H}$   $T_1$  and  $^{19}\text{F}$  spin density contrast images obtained from electrolyte**  
 144 **samples in 5 mm diameter NMR tubes at 20 °C (MPN with (1) 0.05 M  $\text{Co}^{2+}(\text{bpy})_3(\text{TFSI})_2$ , (2) 0.10 M**  
 145  **$\text{Co}^{2+}(\text{bpy})_3(\text{TFSI})_2$ , (3) 0.15 M  $\text{Co}^{2+}(\text{bpy})_3(\text{TFSI})_2$ , (4) 0.05 M  $\text{Co}^{3+}(\text{bpy})_3(\text{TFSI})_3$ , (5) 0.10 M**  
 146  **$\text{Co}^{3+}(\text{bpy})_3(\text{TFSI})_3$ , (6) 0.15 M  $\text{Co}^{3+}(\text{bpy})_3(\text{TFSI})_3$  and (7) both 0.05 M  $\text{Co}^{2+}(\text{bpy})_3(\text{TFSI})_2$  and 0.05 M**  
 147  **$\text{Co}^{3+}(\text{bpy})_3(\text{TFSI})_3$ ). (f) Plot of  $^1\text{H}$   $T_1$  relaxation times (blue circles) of the MPN protons as a function of**  
 148 **temperature and  $\text{Co}^{2+}$  concentration, measured from electrolytes with a total  $\text{Co}(\text{bpy})_3$**   
 149 **concentration of 0.10 M. The surface is a best fit to a polynomial function obtained using MATLAB**  
 150 **(see Supplementary Information for details).**

151

152           The strong dependence of the MPN  $^1\text{H}$   $T_1$  relaxation times on the local concentration of the  
153 cobalt redox species, particularly the paramagnetic  $\text{Co}^{2+}$  state, is clear from Figure 2d. However, these  
154 relaxation times are also temperature dependent (Figure 2f), and both the concentration and  
155 temperature can vary spatially throughout the electrolyte in a functioning thermocell. The  
156 dependence of  $T_1$  on these two variables must therefore be disentangled in order to interpret the  
157 relaxation contrast in a working device. We achieve this by first measuring a  $T_1$  relaxation map of the  
158 thermocell with the temperature gradient applied but the cell in open circuit mode (i.e., electrodes  
159 remaining disconnected). An initial assumption is made that local variations in the concentration of  
160 the redox species are negligible at open circuit voltage, where no external electron transfer occurs to  
161 drive the redox reactions at the electrodes. This allows the acquired  $T_1$  map to be directly converted  
162 to a temperature map via the (independently measured) temperature variation of the  $^1\text{H}$   $T_1$  for the  
163 particular electrolyte used (in this case MPN containing 0.05 M  $\text{Co}^{2+}(\text{bpy})_3(\text{TFSI})_2$  and 0.05 M  
164  $\text{Co}^{3+}(\text{bpy})_3(\text{TFSI})_3$ ). This requires the temperature map to be recorded as quickly as possible after  
165 establishing the thermal gradient in order to minimise the effects of thermophoresis, which can occur  
166 over a time scale of hours (vide infra). Subsequently, an external load resistance is applied and the cell  
167 begins to operate, with both the current and potential continuously measured via the potentiostat. A  
168 second assumption is then made that the resulting redox reactions, accompanying mass transfer  
169 processes such as diffusion and electrophoresis, and other effects such as Joule heating of the  
170 electrodes, do not significantly alter the temperature distribution within the electrolyte, which  
171 remains dominated by conductive and convective heat transfer between the electrodes. This allows  
172 the temperature map obtained from the unconnected cell to be used as a restraint in calculating the  
173 local concentrations of the redox species from subsequent  $T_1$  maps acquired from the functioning cell.  
174 This conversion is achieved using the polynomial function obtained from the surface fit of the  $T_1$  data  
175 in Figure 2f (see Supplementary Information for more details), which were acquired using separate  
176 calibration measurements carried out on individual samples prepared with different  $\text{Co}^{2+}$  and  $\text{Co}^{3+}$   
177 concentrations. We note also that various other assumptions inherent to operando MRI studies of  
178 electrochemical devices also apply, for example that Lorentz forces on the electrolyte ions and eddy  
179 currents on the electrodes play a minimal role in the device functionality.

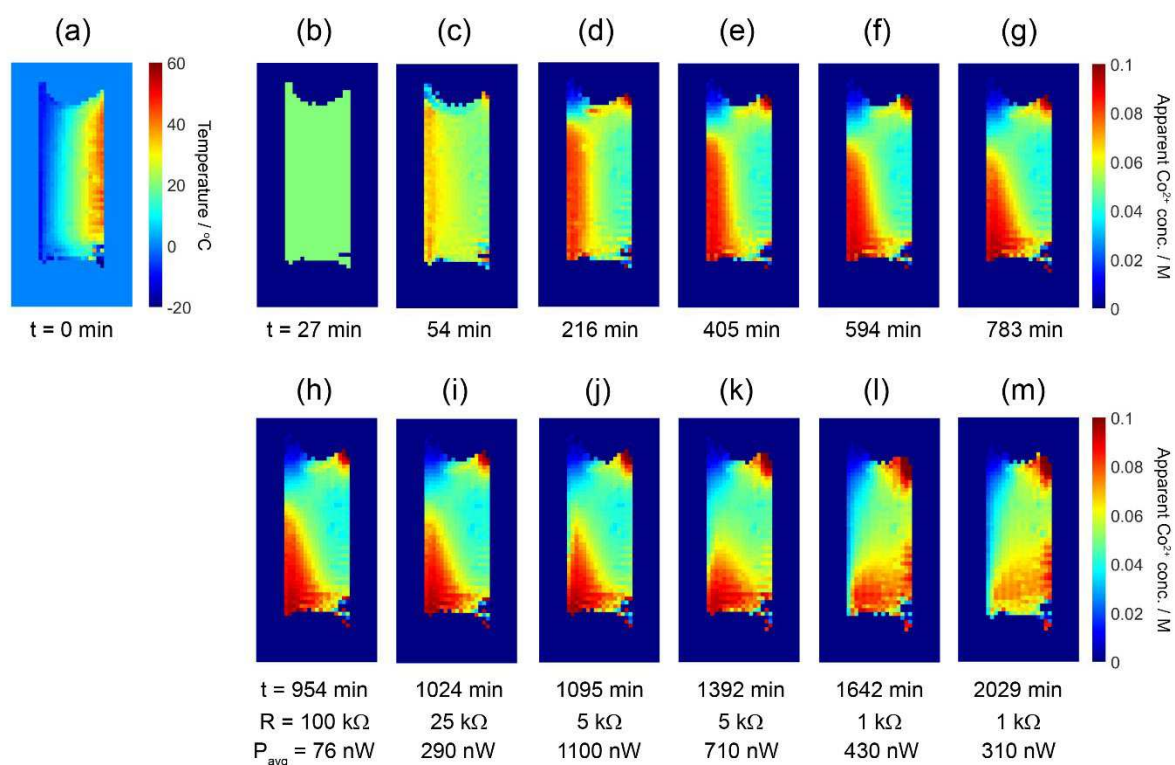


181 **Figure 3 – Temperature maps obtained from the vertical electrode cell containing the MPN with**  
 182 **0.05 M  $\text{Co}^{2+/3+}(\text{bpy})_3(\text{TFSI})_{2/3}$  electrolyte in (a) liquid and (b) gel form. In both cases the target**  
 183 **electrode temperatures were  $-30$  (cold/left) and  $60$  °C (hot/right).**

184

185 **Temperature maps and effects of convection.** Figure 3 shows temperature maps obtained from the  
 186 liquid and gel electrolytes within the vertical electrode cell under an applied temperature differential  
 187 of  $90$  °C (although a narrower actual temperature difference across the electrolyte within the device  
 188 is observed in both cases). In these and all subsequent images presented, the pixel dimensions are  
 189  $0.39 \times 0.39$  mm and the image dimensions are  $12.5 \times 25$  mm. In the liquid (Figure 3a), thermal  
 190 convection acts to continuously circulate the electrolyte in an anti-clockwise direction, resulting in a  
 191 fairly uniform temperature of around  $20$  °C across the majority of the cell, with a cooler region visible  
 192 in the centre of the electrolyte as predicted by modelling [17]. Cold and hot layers are visible close to  
 193 the electrode surfaces, while a hot region is also seen at the top of the hot electrode, possibly trapped  
 194 by the meniscus of the electrolyte. In the gel electrolyte under the same conditions (Figure 3b),  
 195 convection is prevented by the polymer matrix and a more linear temperature gradient is observed  
 196 across the cell. These images provide a stark illustration of the role that convection can play in  
 197 determining the temperature distribution within a thermocell, and the ability of gel electrolytes to  
 198 maintain a large temperature differential by eliminating convective flow.

199



200 **Figure 4 – (a) Temperature map and (b - m) apparent Co<sup>2+</sup> concentration maps obtained from the**  
 201 **vertical electrode cell with the MPN with 0.05 M Co<sup>2+/3+</sup>(bpy)<sub>3</sub>(TFSI)<sub>2/3</sub> gel electrolyte at times**  
 202 **indicated. Images (a – g) were obtained from an unconnected (open circuit) cell. Images (h – m) were**  
 203 **obtained after connecting the load resistances R as indicated. Average powers P<sub>avg</sub> drawn from the**  
 204 **cell during the acquisition of each image are also shown.**

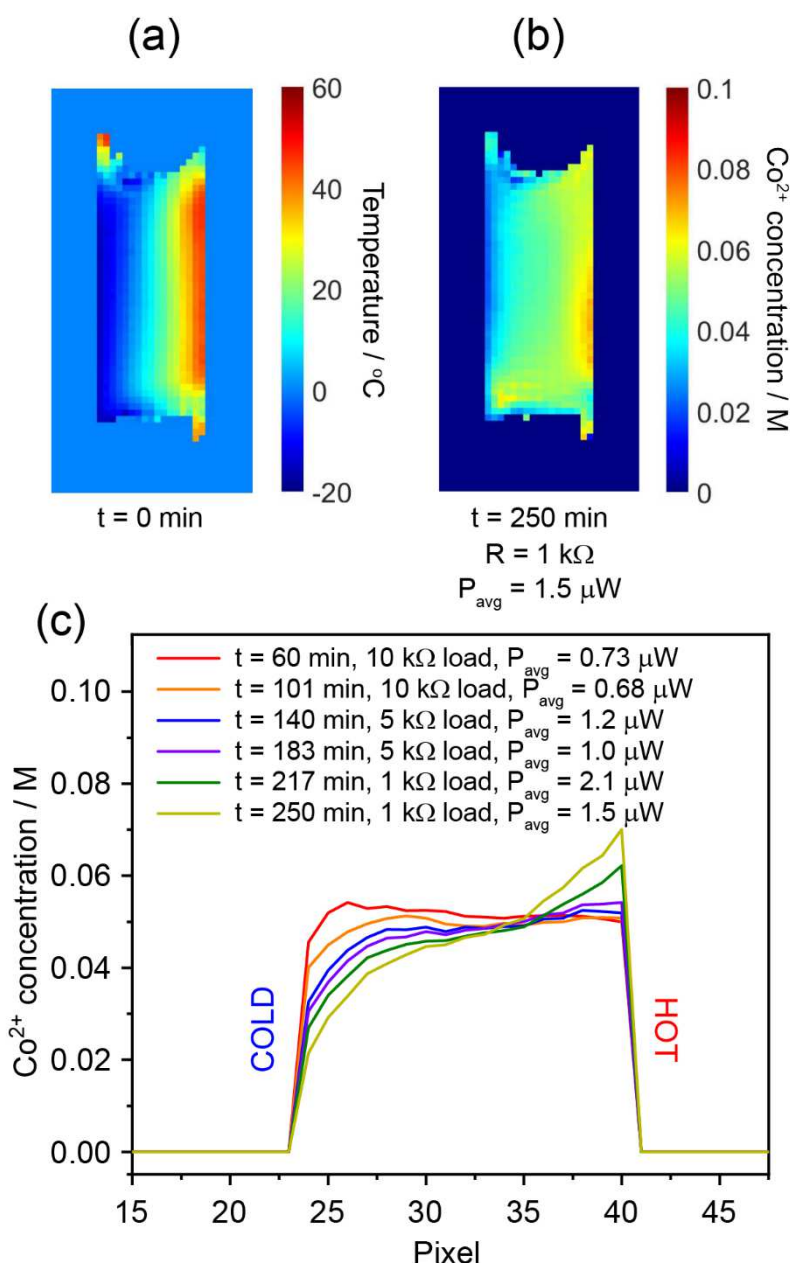
205

206 **Concentration maps and competing mass transfer effects.** For the vertical electrode cell with the gel  
 207 electrolyte, a temperature map and subsequent time-resolved series of concentration maps at open  
 208 circuit voltage and then with different applied load resistances were acquired and are shown in Figure  
 209 4. Each image took approximately 27 min to obtain and the times quoted are the completion times  
 210 for the acquisition of each image. First, Co<sup>2+</sup> concentration maps were obtained from the cell in its  
 211 open circuit state to observe the stability of the electrolyte over time under the effects of the applied  
 212 thermal gradient (Figures 4b to 4g). The initially uniform Co<sup>2+</sup> concentration across the whole  
 213 electrolyte can be seen to change over a period of several hours, with an apparent clustering of Co<sup>2+</sup>  
 214 species on the cold side of the cell (Figure 4d) that eventually begins to sink to the bottom of the  
 215 electrolyte (Figures 4e to 4g). These observed changes are due to thermophoresis, whereby the cobalt  
 216 species (of both oxidation states) migrate towards the cold side of the cell, gradually increasing the  
 217 local electrolyte density and resulting in the sinking effect. Note that this process results in a departure  
 218 of the local net cobalt concentration from 0.10 M, and so the calibration data in Figure 2f no longer

219 applies, hence we have labelled the concentration scale in Figure 4 as “apparent”  $\text{Co}^{2+}$  concentration.  
220 Nonetheless, although these particular images are not truly quantitative, the contrast reliably  
221 illustrates the effects of thermophoresis and the time evolution of the spatial distribution of the cobalt  
222 species within the cell. In a functioning device, the effects of thermophoresis must be overcome by  
223 other mass transfer effects such as diffusion in order for the  $\text{Co}^{3+}$  species to reach the hot electrode  
224 and undergo reduction to  $\text{Co}^{2+}$ . This can be observed in Figures 4h to 4m, in which the cell was  
225 connected to a variable load resistance. Over time, and as the applied load resistance is reduced, the  
226 apparent  $\text{Co}^{2+}$  concentration is seen to increase near the hot electrode, while a layer of reduced  
227 apparent  $\text{Co}^{2+}$  concentration (i.e., increased  $\text{Co}^{3+}$  concentration) grows at the surface of the cold  
228 electrode as expected.

229           Subsequently, a fresh gel electrolyte was placed into the vertical electrode cell and a new  
230 series of concentration maps were generated, this time with the load resistances connected  
231 immediately after recording the temperature map, thereby minimising the effects of thermophoresis.  
232 An example  $\text{Co}^{2+}$  concentration map is shown in Figure 5b, while the evolution of the  $\text{Co}^{2+}$   
233 concentration gradient across the centre of the cell as a function of time and load resistance is shown  
234 in Figure 5c. As the effects of thermophoresis are minimal in this case, these  $\text{Co}^{2+}$  concentration data  
235 are quantitative. The  $\text{Co}^{2+}$  concentration gradient evolves from close to zero in the initial measurement  
236 to a sigmoidal-like profile under the 1 k $\Omega$  load resistance at  $t = 250$  min. This is a departure from the  
237 linear concentration gradients predicted by Sokirko [16], and may be due to a number of factors not  
238 accounted for in the modelling such as the effects of the side walls of the electrolyte chamber, spatial  
239 variations in temperature across the surface of each electrode, and the fact that this system may not  
240 yet have reached the steady state. The concentration map in Figure 5b also shows that the  
241 concentration profile varies vertically across the cell. These temperature and concentration maps  
242 therefore provide valuable experimental data to which modelling results may be compared.

243

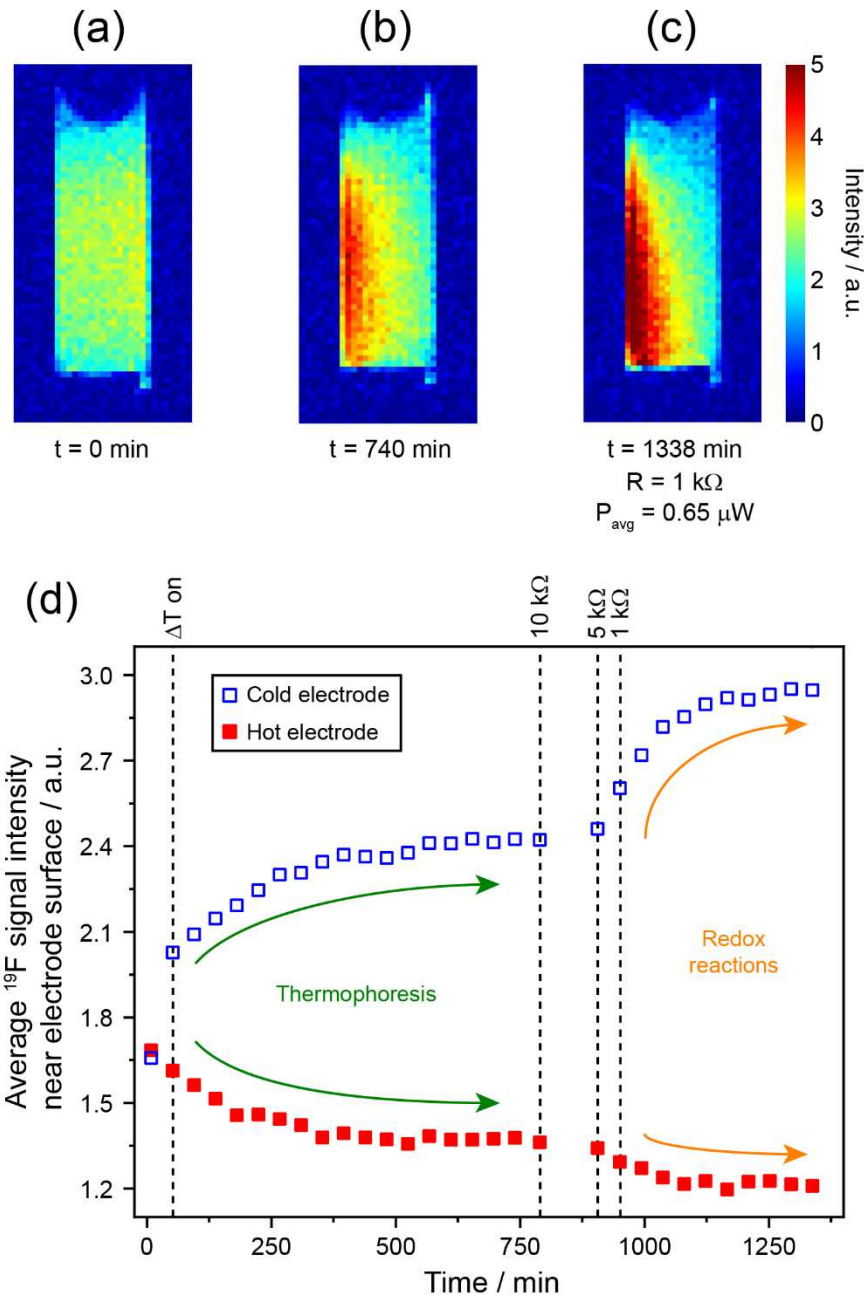


244 **Figure 5 – (a) Temperature map and (b)  $\text{Co}^{2+}$  concentration map obtained from the vertical electrode**  
 245 **cell with the gel electrolyte. (c) One dimensional  $\text{Co}^{2+}$  concentration profiles across the centre of the**  
 246 **cell, extracted from images obtained at the times and under the load resistances indicated (the**  
 247 **yellow plot in (c) was taken from the image in (b)). Average powers  $P_{\text{avg}}$  drawn from the cells during**  
 248 **the acquisition of each image are also quoted. The full series of images are provided in the**  
 249 **Supplementary Information.**

250

251  $^{19}\text{F}$  spin density images of the gel electrolyte in the vertical electrode cell are shown in Figure  
 252 6. These images report on the local concentrations of the TFSI anions, which due to ion clustering will  
 253 in turn depend on the local concentrations of the cobalt redox cations.  $^{19}\text{F}$  image intensity arising from

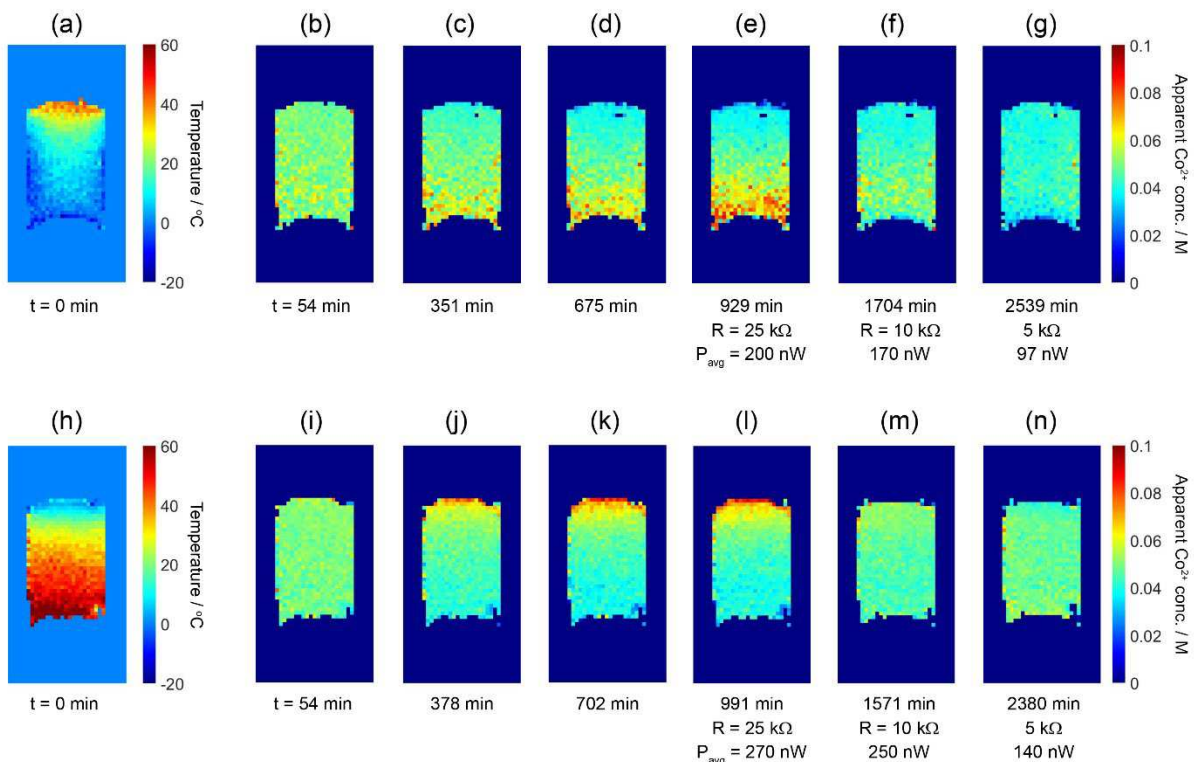
254 the PVDF component of the gel is negligible due to its much broader NMR line width. In the image  
255 obtained from the unconnected cell with no temperature gradient applied (Figure 6a), the spin density  
256 is fairly uniform across the electrolyte as expected. The same thermal gradient as for the  $^1\text{H}$  imaging  
257 experiments discussed above was subsequently applied and after 740 min a clear increase in  $^{19}\text{F}$  spin  
258 density is observed on the cold (left) side of the cell, consistent with the migration of the anions to the  
259 cold side due to thermophoresis. Subsequently, a series of load resistances were applied and the  
260 image in Figure 6c was acquired, showing a further increase in  $^{19}\text{F}$  spin density on the cold side. The  
261 evolutions in image intensities at the electrode surfaces during this series of experiments are plotted  
262 in Figure 6d. Initially, the TFSI concentration increases at the cold electrode and decreases at the hot  
263 electrode due to thermophoresis. When the load resistances are connected, oxidation ( $\text{Co}^{2+} \rightarrow \text{Co}^{3+}$ )  
264 occurs at the surface of the cold electrode, necessitating a further local increase in TFSI concentration  
265 to balance the charge, while the opposite process occurs at the hot electrode. The observation of  
266 larger TFSI concentration changes near the cold electrode (when one might expect the changes at  
267 each electrode to be equal and opposite) is consistent with the predictions of modelling and is due to  
268 the slower rates of diffusion on the cold side of the cell, which leads to more pronounced diffusive  
269 layers at the cold electrode surface (see for example Figure 2c in reference [17]).



270 Figure 6 –  $^{19}\text{F}$  spin density maps obtained from the vertical cell with the gel electrolyte (a) with no  
 271 temperature gradient or load resistance, (b) after 740 min with thermal gradient applied but no load  
 272 resistance connected, and (c) after 1338 min with a  $1\text{ k}\Omega$  load resistance. In (b) and (c), the cold  
 273 electrode is on the left. (d) Time evolution of the  $^{19}\text{F}$  signal intensities at the surface of each electrode  
 274 (average extracted from the four columns of pixels closest to each electrode, corresponding to a  
 275 layer approximately  $1.5\text{ mm}$  thick). The thermal gradient  $\Delta T$  was switched on and the load  
 276 resistances were applied at the times indicated by the dashed lines.

277

278 Finally, a series of  $^1\text{H}$  imaging experiments were carried out on the gel electrolyte in the  
 279 horizontal electrode cell with both hot-above-cold and cold-above-hot configurations (Figure 7).  
 280 Figures 7a and 7h show the acquired temperature maps for these configurations, and the temperature  
 281 gradient is seen to be non-linear and steeper at the top of the cell in both cases. We note some  
 282 distortions to the images which make the top and bottom surfaces appear slightly curved (most  
 283 noticeable for the hot-above cold images in Figures 7a to g), and this is attributed to magnetic field  
 284 inhomogeneities close to the electrodes. For both the hot-above-cold and cold-above-hot  
 285 configurations, the effects of thermophoresis can be observed with an increase in the apparent  $\text{Co}^{2+}$   
 286 concentration appearing over several hours at the cold region of the electrolyte before any load  
 287 resistance is connected. Upon connecting a load resistance, the concentration gradient is gradually  
 288 seen to reverse as other mass transfer processes driven by the redox reactions begin to dominate.  
 289 Average powers  $P_{\text{avg}}$  drawn from the cells during each imaging experiment are around 50% higher for  
 290 the cold-above-hot configuration, indicating a more efficient mass transfer between the electrodes.  
 291 This could be due to some slow or small-scale thermal convection within the gel, and/or the sinking  
 292 of the more dense regions of electrolyte with higher  $\text{Co}^{3+}$  concentration that are formed at the upper  
 293 cold electrode, neither of which would occur for the opposite orientation.



294 **Figure 7 – Temperature and apparent  $\text{Co}^{2+}$  concentration maps for the horizontal electrode cells in**  
 295 **the hot-above-cold (top row) and cold-above-hot (bottom row) configurations. In both cases, the**  
 296 **initial connection to an external load resistance was made at  $t \approx 700$  min.**

297

298 In summary, we have shown that operando MRI can be used to obtain quantitative  
299 temperature and concentration maps from working thermocells, providing valuable experimental  
300 data on the different inter-related processes occurring in these devices that can be correlated with  
301 both modelling results and electrochemical measurements. The inherent paramagnetism of the  $\text{Co}^{2+}$   
302 redox state led to significant  $^1\text{H}$   $T_1$  relaxation contrast, making thermocells particularly well-suited for  
303 characterisation by this technique, and  $^{19}\text{F}$  spin density imaging was also demonstrated as a viable  
304 alternative. We have observed thermophoresis occurring inside a gel electrolyte in an unconnected  
305 cell, and have shown that other mass transfer processes induced by the redox reactions when a load  
306 resistance is applied are dominant over this process and reverse its effects. The image acquisition  
307 times used were short relative to the time scale of the observed concentration changes, allowing them  
308 to be monitored as a function of time and applied load resistance. Other MRI modalities such as  
309 diffusion and velocity mapping will provide further insights into mass transfer processes such as  
310 electrophoresis and convection. The approaches reported herein may also be useful for studying other  
311 energy storage devices such as thermal batteries and capacitors.

312

## 313 **Methods**

314 **Electrolyte preparation.** Reagents for the cobalt redox couple synthetic procedures were purchased  
315 and used as received from Sigma Aldrich, 3M, May & Baker Ltd, Emsure, and LiChrosolv. 3-  
316 Methoxypropionitrile (MPN) (98%) was purchased from Fluka and used as received. The redox couples  
317  $\text{Co}^{2+}(\text{bpy})_3\text{TFSI}_2$  and  $\text{Co}^{3+}(\text{bpy})_3\text{TFSI}_2$  (where  $\text{bpy}$  = 2,2-bipyridyl and  $\text{TFSI}$  = bis(tri-  
318 fluoromethanesulfonyl)imide) were synthesised following a previously published procedure [21].  
319 Polyvinylidene difluoride (PVDF) powder (KF850, molecular weight =  $3 \times 10^5$ ) was purchased from  
320 Kureha Chemicals, Japan, and used as received, and gel electrolytes were prepared by incorporating  
321 5 wt% PVDF into the liquid electrolytes.

322  **$^1\text{H}$  relaxation calibration measurements.** A series of electrolytes with varying fractions of  
323  $\text{Co}^{2+}(\text{bpy})_3\text{TFSI}_2$  and  $\text{Co}^{3+}(\text{bpy})_3\text{TFSI}_2$  but a total  $\text{Co}(\text{bpy})_3$  concentration of 0.10 M were prepared in  
324 both liquid and gel forms.  $^1\text{H}$   $T_1$  relaxation times were measured over a range of sample temperatures  
325 from the MPN signals using an 11.7 T Bruker Avance III standard bore spectrometer, a 5 mm HX  
326 solution-state probe, and a saturation recovery pulse sequence. The resulting data was fitted to a  
327 polynomial surface function (Figure 2) and the resulting parameters of this fit are provided in the  
328 Supplementary Information.

329 **Thermocell designs.** The cells designs were developed in SolidWorks and are available upon request.  
330 Further images of the cells are provided in the Supplementary Information. They were machined from  
331 polyether ether ketone (PEEK) and measure 25 mm in diameter (30 mm diameter cap) and 100 mm in  
332 length. The wider cap at the top allows the cell to rest in the correct position within the imaging probe.  
333 Cell components are connected using PEEK screws with butyl rubber gaskets (1 mm thickness) to  
334 prevent electrolyte leakage. 0.25 mm thick platinum electrodes were also held in place by butyl rubber  
335 gaskets. The surface area of each electrode exposed to the electrolyte was approximately 1.4 cm<sup>2</sup> for  
336 the vertical electrode cell and 0.4 cm<sup>2</sup> for the horizontal electrode cell. For the vertical electrode cell  
337 design, the electrolyte is inserted from above by removing the top cap of the cell. For the horizontal  
338 electrode cells, an inlet on the side of the cell allows the electrolyte to be injected into the cavity  
339 before being sealed with a PEEK screw.

340 **Operando MRI experimental set up.** The cells were placed inside the 25 mm RF coil of a Bruker  
341 Micro2.5 microimaging probe. Separate exchangeable MICWB40 birdcage RF coils were used for <sup>1</sup>H  
342 and <sup>19</sup>F imaging experiments. The hot and cold gas flows were controlled using two independent  
343 Bruker BCU II chiller units. Gas lines and electric cables were connected to the cell before placing the  
344 probe inside a Bruker 11.7 T wide-bore vertical superconducting magnet with an Avance III console  
345 and three GREAT (1/60) amplifiers capable of generating field gradients of up to 1.5 Tm<sup>-1</sup>. In the case  
346 of the vertical electrode configuration, the cell was aligned with the electrode surfaces parallel to the  
347 RF (B<sub>1</sub>) field. The electrode connection cables incorporated an RF filter at the top of the magnet and  
348 were connected to an external BioLogic SP-150 (Science Instruments) potentiostat controlled using  
349 the EC-Lab software, which allowed the applied load resistance to be controlled and the cell potential  
350 and drawn current to be continuously recorded during all imaging experiments. A schematic  
351 illustration of the set-up is provided in the Supplementary Information.

352 **<sup>1</sup>H relaxation mapping.** Imaging experiments were controlled using the Bruker ParaVision software  
353 (v6). The Rapid Acquisition with Relaxation Enhancement (RARE) imaging pulse sequence was used for  
354 all imaging experiments. Images were obtained with a RARE factor of 1, a field of view of 25 × 25 mm  
355 and a matrix dimension of 64 × 64. Vertical slices positioned in the centre of the electrolyte and in a  
356 plane perpendicular to the electrodes were used with slice thicknesses of 8 mm and 5 mm for the  
357 vertical and horizontal electrode configurations respectively. A series of images were obtained using  
358 15 experiments with repetition times logarithmically spaced between 100 and 6000 ms, with a  
359 minimum echo time of 5.08 ms, resulting in a total acquisition time for each T<sub>1</sub> map of 27 minutes.  
360 Signal intensities below a certain threshold (15 – 25%) of the maximum value (i.e., noise outside of  
361 the electrolyte region) were removed. The T<sub>1</sub> maps were then reconstructed from this series of 15  
362 images using the Prospa software (Magritek, New Zealand) by fitting the signal intensity variation of

363 each pixel using the function  $S(t) = S_{max}(1 - e^{-\frac{t}{T_1}})$ , where S(t) is the pixel signal intensity for  
364 repetition time t and  $S_{max}$  is the maximum signal intensity for the pixel.

365 **<sup>19</sup>F spin density imaging.** The <sup>19</sup>F spin density images were also acquired with the RARE pulse  
366 sequence, with a repetition time of 20 s, a RARE factor of 1 and a minimum echo time of 5.08 ms to  
367 minimise relaxation contrast. The slice thickness, field of view and matrix size were identical to the <sup>1</sup>H  
368 imaging, but due to the weaker signal strength additional signal averaging was employed resulting in  
369 an acquisition time of 43 minutes per image.

370 **Data processing.** The <sup>1</sup>H T<sub>1</sub> maps were converted to either temperature or Co<sup>2+</sup> concentration maps  
371 using the relaxation calibration data (see Supplementary Information for full expression) and following  
372 the general procedure outlined in the main text via a home-written MATLAB code. All imaging figures  
373 were generated using MATLAB and cropped in Adobe Illustrator, while data plots were generated  
374 using Origin.

375

## 376 **Acknowledgements**

377 We are grateful to Dr Abuzar Taheri and Dr Ruhamah Yunis for providing the electrolyte samples and  
378 to Mr John Taylor for machining the cells. The Australian Research Council is acknowledged for funding  
379 the microimaging facility via grant LE110100141, and for supporting this research through the ARC  
380 Centre of Excellence for Electromaterials Science (ACES).

381

## 382 **Author contributions**

383 I.E.G. and L.A.O. conceived the project. I.E.G. designed the cells, carried out the experiments and data  
384 analysis, led the data interpretation and assisted with the paper writing. J.M.P. and M.F. assisted with  
385 the project execution, data interpretation and paper writing. L.A.O. assisted with the project execution  
386 and data interpretation, and wrote the paper.

387

## 388 **Competing interests**

389 The authors declare no competing interests.

390

## 391 **Additional information**

392 **Supplementary Information** (Additional cell drawings, experimental set up schematic, <sup>1</sup>H NMR  
393 spectrum of the electrolyte, polynomial function details, additional images)

394

## 395 **References**

396 [1] C. Forman, I.K. Muritala, R. Pardemann and B. Meyer, Estimating the global waste heat  
397 potential, *Renew. Sustain. Energy Rev.* 57 (2016) 1568-1579

398 [2] M.F. Dupont, D.R. MacFarlane and J.M. Pringle, Thermo-electrochemical cells for waste heat  
399 harvesting – progress and perspectives, *Chem. Commun.* 53 (2017) 6288-6302

400 [3] M. Li, M. Hong, M. Dargusch, J. Zou and Z-G. Chen, High-Efficiency Thermocells Driven by  
401 Thermo-Electrochemical Processes, *Trends in Chemistry* DOI: 10.1016/j.trechm.2020.11.001

402 [4] J.T. Hupp and M.J. Weaver, Solvent, ligand, and ionic charge effects on reaction entropies  
403 for simple transition-metal redox couples, *Inorg. Chem.* 23 (1984) 3639-3644

404 [5] P. Yang, K. Liu, Q. Chen, X. Mo, Y. Zhou, S. Li, G. Feng and J. Zhou, Wearable Thermocells  
405 Based on Gel Electrolytes for the Utilization of Body Heat, *Angew. Chem.* 128 (2016) 12229-  
406 12232

407 [6] Y. Liu, S. Zhang, Y. Zhou, M.A. Buckingham, L. Aldous, P.C. Sherrell, G.G. Wallace, G. Ryder, S.  
408 Faisal, D.L. Officer, S. Beirne and J. Chen, Advanced Wearable Thermocells for Body Heat  
409 Harvesting, *Adv. Energy Mater.* 10 (2020) 2002539

410 [7] C.-G. Han, X. Qian, Q. Li, B. Deng, Y. Zhu, Z. Han, W. Zhang, W. Wang, S.-P. Feng, G. Chen and  
411 W. Liu, Giant thermopower of ionic gelatin near room temperature, *Science* 368 (2020)  
412 1091-1098

413 [8] L. Zhang, T. Kim, N. Li, T.J. Kang, J. Chen, J.M. Pringle, M. Zhang, A.H. Kazim, S. Fang, C.  
414 Haines, D. Al-Masri, B.A. Cola, J.M. Razal, J. Di, S. Beirne, D.R. MacFarlane, A. Gonzalez-  
415 Martin, S. Mathew, Y.H. Kim, G. Wallace and R.H. Baughman, High Power Density  
416 Electrochemical Thermocells for Inexpensively Harvesting Low-Grade Thermal Energy, *Adv.*  
417 *Mater.* 29 (2017) 1605652

418 [9] H. Zhou and P. Liu, High Seebeck Coefficient Electrochemical Thermocells for Efficient Waste  
419 Heat Recovery, *ACS Appl. Energy Mater.* 1 (2018) 1424-1428

420 [10] T. Shibata, H. Iwaizumi, Y. Fukuzumi and Y. Morimoto, Energy harvesting thermocell with use  
421 of phase transition, *Sci. Rep.* 10 (2020) 1813

422 [11] B. Yu, J. Duan, H. Cong, W. Xie, R. Liu, X. Zhuang, H. Wang, B. Qi, M. Xu, Z.L. Wang and J.  
423 Zhou, Thermosensitive crystallization-boosted liquid thermocells for low-grade heat  
424 harvesting, *Science* 370 (2020) 342-346

425 [12] H. Im, T. Kim, H. Song, J. Choi, J.S. Park, R. Ovalle-Robles, H.D. Yang, K.D. Kihm, R.H.  
426 Baughman, H.H. Lee, T.J. Kang and Y.H. Kim, High-efficiency electrochemical thermal energy  
427 harvester using carbon nanotube aerogel sheet electrodes, *Nature Commun.* 7 (2016) 10600

428 [13] D.R. MacFarlane, M. Forsyth, P.C. Howlett, M. Kar, S. Passerini, J.M. Pringle, H. Ohno, M.  
429 Watanabe, F. Yan, W. Zheng, S. Zhang and J. Zhang, Ionic liquids and their solid-state  
430 analogues as materials for energy generation and storage, *Nature Rev. Mater.* 1 (2016)  
431 15005

- 432 [14] J. Duan, G. Feng, B. Yu, J. Li, M. Chen, P. Yang, J. Feng, K. Liu and J. Zhou, Aqueous  
433 thermogalvanic cells with a high Seebeck coefficient for low-grade heat harvest, *Nature*  
434 *Commun.* 9 (2018) 5146
- 435 [15] J.H. Kim, J.H. Lee, R.R. Palem, M.-S. Suh, H.H. Lee and T.J. Kang, Iron (II/III) perchlorate  
436 electrolytes for electrochemically harvesting low-grade thermal energy, *Sci. Rep.* 9 (2019)  
437 8706
- 438 [16] A.V. Sokirko, Theoretical study of thermogalvanic cells in steady state, *Electrochim. Acta* 39  
439 (1994) 597-609
- 440 [17] P.F. Salazar, S. Kumar and B.A. Cola, Design and optimization of thermo-electrochemical cells,  
441 *J. Appl. Electrochem.* 44 (2014) 325-336
- 442 [18] M.A. Buckingham and L. Aldous, Thermogalvanic cells: A side-by-side comparison of  
443 measurement methods, *J. Electroanal. Chem.* 872 (2020) 114280
- 444 [19] T.I. Quickenden and Y. Mua, The Power Conversion Efficiencies of a Thermogalvanic Cell  
445 Operated in Three Different Orientations, *J. Electrochem. Soc.* 142 (1995) 3652-3659
- 446 [20] A. Gunawan, H. Li, C.-H. Lin, D.A. Buttry, V. Mujica, R.A. Taylor, R.S. Prasher and P.E. Phelan,  
447 The amplifying effect of natural convection on power generation of thermogalvanic cells, *Int.*  
448 *J. Heat Mass Transfer* 78 (2014) 423-434
- 449 [21] T.J. Abraham, D.R. MacFarlane and J.M. Pringle, High Seebeck coefficient redox ionic liquid  
450 electrolytes for thermal energy harvesting, *Energy Environ. Sci.* 6 (2013) 2639-2645
- 451 [22] N. Jiao, T.J. Abraham, D.R. MacFarlane and J.M. Pringle, Ionic Liquid Electrolytes for Thermal  
452 Energy Harvesting Using a Cobalt Redox Couple, *J. Electrochem. Soc.* 161 (2014) D3061-  
453 D3065
- 454 [23] A. Taheri, D.R. MacFarlane, C. Pozo-Gonzalo and J.M. Pringle, Quasi-solid-State Electrolytes  
455 for Low-Grade Thermal Energy Harvesting using a Cobalt Redox Couple, *Chem. Sus. Chem.*  
456 11 (2018) 2788-2796
- 457 [24] A. Taheri, D.R. MacFarlane, C. Pozo-Gonzalo and J.M. Pringle, Flexible and non-volatile redox  
458 active quasi-solid state ionic liquid based electrolytes for thermal energy harvesting, *Sus.*  
459 *Energy Fuels* 2 (2018) 1806-1812
- 460 [25] S.W. Hasan, S.M. Said, M.F.M. Sabri, A.S.A. Bakar, N.A. Hashim, M.M.I.M. Hasnan, J.M. Pringle  
461 and D.R. MacFarlane, High Thermal Gradient in Thermoelectrochemical Cells by Insertion of a  
462 Poly(Vinylidene Fluoride) Membrane, *Sci. Rep.* 6 (2016) 29328
- 463 [26] A.J. Ilott, N.M. Trease, C.P. Grey and A. Jerschow, Multinuclear in situ magnetic resonance  
464 imaging of electrochemical double-layer capacitors, *Nature Commun.* 5 (2014) 4536
- 465 [27] M. Mohammadi and A. Jerschow, In situ and operando magnetic resonance imaging of  
466 electrochemical cells: A perspective, *J. Magn. Reson.* 308 (2019) 106600
- 467 [28] M. M. Britton, Magnetic Resonance Imaging of Electrochemical Cells Containing Bulk Metal,  
468 *Chem. Phys. Chem.* 15 (2014) 1731-1736
- 469 [29] S.A. Krachkovskiy, J.M. Foster, J.D. Bazak, B.J. Balcom and G.R. Goward, Operando Mapping of  
470 Li Concentration Profiles and Phase Transformations in Graphite Electrodes by Magnetic  
471 Resonance Imaging and Nuclear Magnetic Resonance Spectroscopy, *J. Phys. Chem. C* 122  
472 (2018) 21784-21791

- 473 [30] K. Romanenko, L. Jin, P. Howlett and M. Forsyth, In Situ MRI of Operating Solid-State Lithium  
474 Metal Cells Based on Ionic Plastic Crystal Electrolytes, *Chem. Mater.* 28 (2016) 2844-2851
- 475 [31] S.A. Krachkovskiy, J.D. Bazak, P. Werhun, B.J. Balcom, I.C. Halalay and G.R. Goward,  
476 Visualization of Steady-State Ionic Concentration Profiles Formed in Electrolytes during Li-Ion  
477 Battery Operation and Determination of Mass-Transport Properties by in Situ Magnetic  
478 Resonance Imaging, *J. Am. Chem. Soc.* 138 (2016) 7992-7999
- 479 [32] M.M. Britton, P.M. Bayley, P.C. Howlett, A.J. Davenport and M. Forsyth, In Situ, Real-Time  
480 Visualization of Electrochemistry Using Magnetic Resonance Imaging, *J. Phys. Chem. Lett.* 4  
481 (2013) 3019-3023
- 482 [33] A.J. Ilott, M. Mohammadi, C.M. Schauerman, M.J. Ganter and A. Jerschow, Rechargeable  
483 lithium-ion cell state of charge and defect detection by in-situ inside-out magnetic resonance  
484 imaging, *Nature Commun.* 9 (2018) 1776
- 485 [34] M. Mohammadi, E.V. Silletta, A.J. Ilott and A. Jerschow, Diagnosing current distributions in  
486 batteries with magnetic resonance imaging, *J. Magn. Reson.* 309 (2019) 106601
- 487 [35] J.M. Bray, C.L. Doswell, G.E. Pavlovskaya, L. Chen, B. Kishore, H. Au, H. Alptekin, E. Kendrick,  
488 M.-M. Titirici, T. Meersmann and M.M. Britton, Operando visualisation of battery chemistry  
489 in a sodium-ion battery by  $^{23}\text{Na}$  magnetic resonance imaging, *Nature Commun.* 11 (2020) 2083
- 490 [36] A.J. Ilott, M. Mohammadi, H.J. Chang, C.P. Grey and A. Jerschow, Real-time 3D imaging of  
491 microstructure growth in battery cells using indirect MRI, *Proc. Nat. Acad. Sci.* 113 (2016)  
492 10779-10784
- 493 [37] S. Benders, B.F. Gomes, M. Carmo, L.A. Colnago and B. Blümich, *In-situ* MRI velocimetry of the  
494 magnetohydrodynamic effect in electrochemical cells, *J. Magn. Reson.* 312 (2020) 106692
- 495 [38] A.J. Pell, G. Pintacuda and C.P. Grey, Paramagnetic NMR in solution and the solid state,  
496 *Progress Nucl. Magn. Reson. Spec.* 111 (2019) 1-271

## Supplementary Files

This is a list of supplementary files associated with this preprint. Click to download.

- [OperandoMRIofthermocellsSI.pdf](#)